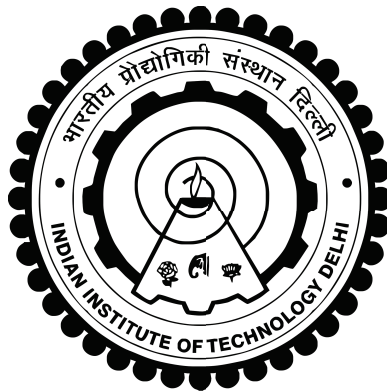


**GLAUCOMA DIAGNOSIS IN A DIGITAL RETINAL
IMAGE USING MULTI CLINICAL FEATURES
EXTRACTED AND FUSED BY DEEP CONVOLUTIONAL
NEURAL NETWORKS**

AMBIKA SHARMA



**BHARTI SCHOOL OF TELECOMMUNICATION
TECHNOLOGY AND MANAGEMENT
INDIAN INSTITUTE OF TECHNOLOGY DELHI**

July 2022

**GLAUCOMA DIAGNOSIS IN A DIGITAL RETINAL
IMAGE USING MULTI CLINICAL FEATURES
EXTRACTED AND FUSED BY DEEP CONVOLUTIONAL
NEURAL NETWORKS**

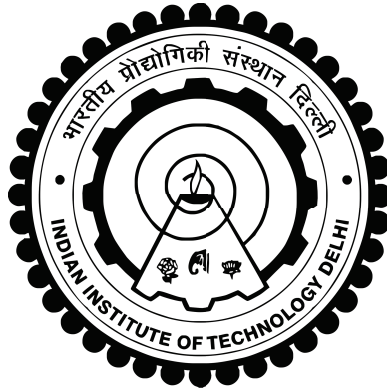
by

**AMBIKA SHARMA
BHARTI SCHOOL OF TELECOMMUNICATION
TECHNOLOGY AND MANAGEMENT**

Submitted

in fulfillment of the requirements of the degree of DOCTOR OF
PHILOSOPHY

to the



**Indian Institute of Technology Delhi
July 2022**

CERTIFICATE

This is to certify that the thesis entitled, “**GLAUCOMA DIAGNOSIS IN A DIGITAL RETINAL IMAGE USING MULTI CLINICAL FEATURES EXTRACTED AND FUSED BY DEEP CONVOLUTIONAL NEURAL NETWORKS**” being submitted by **Ms. Ambika Sharma** for the award of the degree of **Doctor of Philosophy** is a record of bonafide research work carried out by him in the Bharti School of Telecommunication Technology and Management of Indian Institute of Technology Delhi.

Ms. Ambika Sharma has worked under my guidance and supervision and has fulfilled the requirements for the submission of this thesis, which to my knowledge has reached the requisite standard. The results obtained here in have not been submitted to any other University or Institute for the award of any degree.

Date: 01-07-2022

monika

Prof. Monika Aggarwal

Center of Applied Research in Electronics

Indian Institute of Technology Delhi

New Delhi-110016, India



Prof. Sumantra Dutta Roy

Electrical Engineering

Indian Institute of Technology Delhi

New Delhi-110016, India

Vivek Gupta

Dr. Vivek Gupta

Community Ophthalmology

All India Institute of Medical Sciences (AIIMS)

New Delhi-110029, India

ACKNOWLEDGEMENTS

I offer my deepest gratitude and indebtedness to **Prof. Monika Aggarwal**, **Prof. Sumantra Dutta Roy** and **Dr. Vivek Gupta** for providing me an opportunity to carry out the Ph.D. work under their supervision at IIT Delhi. It is a privilege to work with a person who can guide your research and also train you to for all the aspects which Ph.D. entails. I learned dedication and perseverance from Prof. Monika, which always inspired me. Her deep involvement, care, and guidance for students are beyond words to express. Moreover, Prof. Sumantra out of the box ideas and technical suggestions have helped me during my Ph.D. work in dealing with complex problems and situations. I would also like to thank Dr. Praveen Vashisht, Dr. Talvir Sidhu from the All India Institute of Medical Sciences, Delhi for their valuable clinical suggestions as well as support for my research work. Their intuitive inputs have provided me with a different perspective of looking into the research problems.

I wish to convey my sincere thanks to Prof. Arun Kumar, Prof. S. D. Joshi, Prof. Brijesh Lall, and Prof. Deepak U. Patil for their valuable inputs during my course work, which made the foundation for my research work.

Once again, I am grateful to IIT Delhi for providing me with the research facilities. I am extremely thankful to Mr. Purushottam Das and Mrs. Sneha Menchanda of the Signal processing lab for providing me facilities and assistance during this work. I would also like to thank my Lab mates, Dr. Payal Gupta, Mr. Bipin Kumar, Mrs. Kamini Upadhyay, Mr. Surya Prakash Sankuru, Ms. Jyothi, and Mr. Ritesh Kumar. I also like to thank my friends Mr. Utkarsh Sharma, Ms. Pooja Sarin, Mr. Ashish Dora, Dr. Vijay, Dr. Nidhi Kaur and Mrs. Deepika Kumari. I am likewise thankful to those who have directly or indirectly me to finish my dissertation study.

Last but not least, I like to thank my beloved family for their love and support throughout the journey. No amount of thanks and credit is sufficient enough to reflect what my father Dr. Dharam Pal Sharma has sacrificed to bring me to this state at expense of his own growth. I do not find words to thank my mother Mrs. Sudershana Devi for the love, care, and support that she has given me all my life. I would like to thank them for allowing me to progress on the path of research while not being bothered by my duties as a daughter. I wish to thank my brother Sangam Sharma for being supportive and motivating me during my Ph.D. work. It is giving me immense

joy to thank my cousins Anchal, Atish, Surbhi, Parul, and Poonam for providing me the moral guidance. I also like to thank my elders Mrs. Indu Devi, Dr. Ashok Kumar Sharma and Dr. Prabha Sharma for being supportive throughout my journey.

At last, I feel extremely thankful to almighty for giving such a life where I have been able to make choices that I have made and pursue the goal of higher knowledge and wisdom.

ABSTRACT

The advancement in computerized medical imaging has pushed the boundaries of many researchers to develop automated algorithms for disease diagnosis without human intervention. Glaucoma diagnosis among various eye diseases has remained a major challenge in the medical field. The lack of trained specialists and large patient to ophthalmologist ratio, have motivated us to develop cost-effective computer-based diagnostic systems that can assist medical experts in early diagnosis and aid in reducing their time and effort on healthy scenarios. In the glaucoma prediction procedure, ophthalmologists analyze the retinal image for various eye pathologies such as increased cup-to-disc ratio (CDR), neuro-retinal rim (NRR) loss, peripapillary atrophy (PPA), retinal nerve fiber layer (RNFL) loss, disc asymmetry, etc. Through this thesis, we exploit many clinical indicators along with the recent deep convolutional neural networks for better feature learning.

Regarding the methodology, the first contribution proposes an automatic detection and segmentation of one of the major retinal landmarks i.e., optic disc. Using the location and intensity profile of the optic disc, a DI map is predicted using a U-net architecture and OD is located with the LoG operator. Following this, a Generative adversarial network is proposed to segment the disc boundary. A well-defined study is performed among retinal datasets to validate the model performance. The second contribution of this thesis is to use a multi-encoder U-net framework for optic cup segmentation which significantly outperforms the state-of-the-art. The third contribution detects the two major clinical indicators i.e., PPA and RNFL, of glaucoma using two breakthrough techniques (Transfer and Active Learning) of deep learning. We formulate a novel PPA detection algorithm using a fusion of statistical features and high-level features from a pre-trained deep CNN. Further, we propose an Active transfer learning framework for patch-level classification of RNFL loss. We show encouraging results in comparison to state of art and are able to handle well low dataset scenarios. The fourth contribution of the thesis proposes an automatic glaucoma detection algorithm using ensemble learning of various clinical signs (PPA, RNFL), an SVM-based prediction model using cup and disc extracted features like CDR, ISNT ratio, and finally deep pre-trained CNN-based prediction model. We perform a robust set of experiments to validate the algorithm under all pathological conditions.

This thesis presents localization, segmentation, and classification techniques for medical images and can be applied to other applications. The proposed algorithms have been validated on public standard datasets, such as Drishti-GS, Origa, Refugee, and a private community camp-based challenging dataset collected from the All India Institute of Medical Sciences (AIIMS), Delhi. In conclusion, we have shown encouraging results for disease identification. Ensemble learning with clinically significant features and a deep CNN is a novel approach for glaucoma.

सार

कम्प्यूटरीकृत चिकित्सा इमेजिंग में प्रगति ने मानव हस्तक्षेप के बिना रोग निदान के लिए स्वचालित एल्गोरिदम विकसित करने के लिए कई शोधकर्ताओं की सीमाओं को प्रोत्साहित किया है। विभिन्न नेत्र रोगों में ग्लूकोमा का निदान चिकित्सा क्षेत्र में एक बड़ी चुनौती बना हुआ है। प्रशिक्षित विशेषज्ञों की कमी और नेत्र रोग विशेषज्ञ अनुपात के लिए बड़े रोगी ने हमें लागत प्रभावी कंप्यूटर-आधारित निदान प्रणाली विकसित करने के लिए प्रेरित किया है जो चिकित्सा विशेषज्ञों को प्रारंभिक निदान में सहायता कर सकता है और स्वस्थ परिदृश्यों पर उनके समय और प्रयास को कम करने में सहायता कर सकता है। ग्लूकोमा भविष्यवाणी प्रक्रिया में, नेत्र रोग विशेषज्ञ विभिन्न नेत्र विकृति के लिए रेटिना छवि का विश्लेषण करते हैं जैसे कि कप-टू-डिस्क अनुपात (सीडीआर), न्यूरो-रेटिनल रिम (एनआरआर) हानि, पेरिपैपिलरी एट्रोफी (पीपीए), रेटिना तंत्रिका फाइबर परत (आरएनएफएल) हानि, डिस्क विषमता, आदि। इस शोध प्रबंध के अंतर्गत, हम बेहतर विशेषताएँ सीखने के लिए नवीनतम गहरे दृढ़ तंत्रिका संजाल के साथ-साथ कई नैदानिक संकेतकों का फायदा उठाते हैं।

कार्यप्रणाली के संबंध में, पहला योगदान प्रमुख रेटिनल लैंडमार्क यानी ऑप्टिक डिस्क में से एक का स्वचालित पता लगाने और विभाजन का प्रस्ताव करता है। ऑप्टिक डिस्क के स्थान और तीव्रता प्रोफाइल का उपयोग करते हुए, यू-नेट आर्किटेक्चर का उपयोग करके एक DI मानचित्र की भविष्यवाणी की जाती है और OD LoG ऑपरेटर के साथ स्थित होता है। इसके बाद, डिस्क सीमा को खंडित करने के लिए एक जनरेटिव प्रतिकूल संजाल का प्रस्ताव है। मॉडल प्रदर्शन को मान्य करने के लिए रेटिना डेटासेट के बीच एक अच्छी तरह से परिभाषित अध्ययन किया जाता है। इस शोध प्रबंध का दूसरा योगदान ऑप्टिक कप सेगमेंटेशन के लिए एक मल्टी-एनकोडर यू-नेट फ्रेमवर्क का उपयोग करना है जो अत्याधुनिक रूप से बेहतर प्रदर्शन करता है। तीसरा योगदान दो प्रमुख नैदानिक संकेतकों यानी पीपीए और आरएनएफएल का पता लगाता है, गहन शिक्षा की दो सफलता तकनीकों (ट्रांसफर और एक्टिव लर्निंग) का उपयोग करके ग्लूकोमा के। हम एक पूर्व-प्रशिक्षित गहरे सीएनएन से सांख्यिकीय विशेषताओं और उच्च-स्तरीय सुविधाओं के संलयन का उपयोग करके

एक उपन्यास पीपीए डिटैक्शन एल्गोरिदम तैयार करते हैं। इसके अलावा, हम आरएनएफएल नुकसान के पैच-स्तरीय वर्गीकरण के लिए एक सक्रिय हस्तांतरण सीखने की रूपरेखा का प्रस्ताव करते हैं। हम अत्याधुनिक की तुलना में उत्साहजनक परिणाम दिखाते हैं और कम डेटासेट परिदृश्यों को संभालने में सक्षम हैं। शोध प्रबंध का चौथा योगदान विभिन्न नैदानिक संकेतों (पीपीए, आरएनएफएल) के पहनावा सीखने का उपयोग करते हुए एक स्वचालित ग्लूकोमा डिटैक्शन एल्गोरिदम का प्रस्ताव करता है, एक एसवीएम-आधारित भविष्यवाणी मॉडल जिसमें सीडीआर, आईएसएनटी अनुपात और अंत में गहन पूर्व-प्रशिक्षित सीएनएन जैसे कप और डिस्क निकाले गए सुविधाओं का उपयोग किया जाता है। आधारित भविष्यवाणी मॉडल। हम सभी रोग स्थितियों के तहत एल्गोरिथम को मान्य करने के लिए प्रयोगों का एक मजबूत सेट करते हैं।

यह शोध प्रबंध चिकित्सा छवियों के लिए स्थानीयकरण, विभाजन और वर्गीकरण तकनीकों को प्रस्तुत करता है और अन्य अनुप्रयोगों पर लागू किया जा सकता है। प्रस्तावित एल्गोरिदम को सार्वजनिक मानक डेटासेट, जैसे ट्रि-जीएस, ओरिगा, रिफ्यूजी, और अखिल भारतीय आयुर्विज्ञान संस्थान (एम्स), दिल्ली से एकत्र किए गए एक निजी समुदाय शिविर-आधारित चुनौतीपूर्ण डेटासेट पर मान्य किया गया है। अंत में, हमने रोग की पहचान के लिए उत्साहजनक परिणाम दिखाए हैं। नैदानिक रूप से महत्वपूर्ण विशेषताओं के साथ सीखना और गहन सीएनएन ग्लूकोमा के लिए एक नया दृष्टिकोण है।

TABLE OF CONTENTS

	Page
Certificate	i
Acknowledgments	ii
Abstract	iv
Abstract (Hindi)	vi
List of Figures	xi
List of Tables	xxiii
List of Abbreviations	xxviii
CHAPTER - I INTRODUCTION	1
1.1 Statistics of Eye Diseases	1
1.2 Anatomical Structure of Human Eye	5
1.2.1 Structure of Eye	5
1.2.2 Retinal (Fundus) Image Analysis	8
1.3 Glaucoma Eye Disease	10
1.3.1 Clinical Methods for Glaucoma Diagnoses	16
1.3.2 Clinical Features of Glaucomatous Optic Nerve Damage	17
1.4 Challenges in Automated Glaucoma Diagnosis	22
1.4.1 Large Volume of Clinical Data for Research Purpose	23
1.4.2 Imaging Artefacts and Poor Resolution Images	24
1.4.3 Labelling of Ground-truth Data by Experts	24
1.4.4 Retinal Image Acquisition Procedure	25
1.4.5 Unbalanced Data and Security Issues	25
1.5 Problem Categorization	26
1.6 Motivation	27
1.7 Contributions	28
1.8 Thesis Layout	29
CHAPTER - II LITERATURE REVIEW	32
2.1 Introduction	32
2.2 Optic Disc Detection Algorithms	32
2.2.1 Image Processing based Techniques	32
2.2.2 Deep Learning based Techniques	36
2.3 Optic Disc segmentation Techniques	37
2.3.1 Image Processing and Computer Vision based OD Segmentation Approaches	37
2.3.2 Deep Learning based OD Segmentation Approaches	39
2.4 Optic Cup Segmentation Approaches	40

2.4.1	Image processing based OC Segmentation Algorithms	40
2.4.2	Machine Learning Techniques for OC Segmentation	43
2.5	Glaucoma Diagnosis Methods	43
2.5.1	Clinical Feature based Classification	44
2.5.2	Deep Neural Network Feature based Classification	46
2.6	Peripapillary Atrophy Detection Techniques	47
2.7	Retinal Nerve Fiber Layer (RNFL) Loss Detection Methods	48
2.8	Conclusion	49
 CHAPTER - III OPTIC DISC LOCALIZATION/DETECTION AND SEGMENTATION FROM DIGITAL FUNDUS IMAGES		
		51
3.1	Introduction	51
3.2	The Work in Perspective	53
3.3	Problem Formulation	54
3.4	Optic Disc Localization	55
3.4.1	A U-Net-based Distance-Intensity (DI) Map for OD Localization	55
3.4.1.1	DI Maps from Normalized Distance and Intensity Maps	56
3.4.1.2	DI Map Estimation (or Generation) using U-net Architecture	57
3.4.1.3	A Robust Loss Function to handle Artefacts, Exudates and other Clinical Pathological Regions	58
3.4.1.4	gLoG-based OD Localization on the Estimated DI map	60
3.5	Optic Disc Segmentation	60
3.5.1	Method 1: Anatomical Atlases with Nonrigid Registration	61
3.5.1.1	CBIR Model from the Fundus Atlas for Inter-Image Matching	61
3.5.1.2	SIFT-Flow Deformable Warping of OD Atlas	64
3.5.1.3	Thresholding with Mask Smoothing	65
3.5.2	Method 2: Generative Adversarial Networks	67
3.5.2.1	Pre-processing	67
3.5.2.2	Generative Adversarial Network for Optic Disc Segmentation	68
3.5.2.3	Loss Function of GAN	69
3.5.2.4	Post-processing	71
3.6	Experiments and Results	71
3.6.1	Optic Disc Detection Experiments	72
3.6.1.1	Datasets	72
3.6.1.2	Implementation Details	72

3.6.1.3	Gamma and Beta Parameter Evaluation	75
3.6.1.4	Tukey’s biweight loss function implementation	75
3.6.1.5	Robust OD Detection for Wide Variety of Query Images: Blur, Poor Illumination, Pathology Artefacts	77
3.6.1.6	Evaluated Results for OD Detection	78
3.6.2	Optic Disc Segmentation Experiments	81
3.6.2.1	Method 1: Experiments and Results	81
3.6.2.2	Method 2: Experiments and Results	83
3.7	Conclusions	91
 CHAPTER - IV BETTER FEATURE EXTRACTION USING MULTI- -ENCODER CONVOLUTIONAL NEURAL NETWO- -RKS FOR OPTIC CUP SEGMENTATION FROM DIGITAL FUNDUS IMAGES		94
4.1	Introduction	94
4.2	The Work in Perspective	96
4.3	Proposed Method	96
4.3.1	Pre-processing and Augmentation	97
4.3.2	Model Architectures	98
4.3.2.1	Standard Convolutional Networks	99
4.3.2.2	Y-net Architectures	99
4.3.3	Feature Fusion Bottleneck Blocks	101
4.3.3.1	Inception Block	101
4.3.3.2	Multi-Receptive Field Context Block	101
4.3.4	Decoder Network	102
4.4	Experiments and Results	102
4.4.1	Database Acquisition	103
4.4.2	Evaluation Metrics	103
4.4.3	Implementation Details	104
4.4.4	Comparison with Other Methods	106
4.4.5	Observations of the Research	107
4.5	Conclusions	109
 CHAPTER - V PERIPAPILLARY ATROPHY AND RETINAL NERVE FIBER LAYER LOSS DETECTION		110
5.1	Introduction	110
5.2	The Work in Perspective	112
5.3	Proposed Methodology	113
5.3.1	PPA Detection	113

5.3.1.1	Pre-processing Steps	114
5.3.1.2	Fusion of Deep and Clinically Significant Features for PPA Detection	116
5.3.1.3	Deep Learning-based Models	117
5.3.1.4	Clinically Significant Statistical Handcrafted Features	121
5.4	Methodology for RNFL Detection	122
5.4.1	Pre-processing Steps	123
5.4.1.1	Blood Vessel Extraction and Inpainting	124
5.4.1.2	Patch Generation and Augmentation	124
5.4.2	Deep Active Transfer Learning (ATL) based RNFL Defect Analysis	125
5.4.3	Retinal Image Level RNFL Classification	126
5.5	Experiments and Results	127
5.5.1	PPA Experiments	127
5.5.1.1	Dataset	128
5.5.1.2	Augmentation	129
5.5.1.3	Experiments with a Wide Variety of PPA Images: Poor Illumination, Blurriness and Noise	129
5.5.1.4	Implementation Details	131
5.5.1.5	Comparison with other Approaches	135
5.5.2	RNFL experiments	136
5.5.2.1	Dataset	136
5.5.2.2	Active Learning Method Analysis for Classification	137
5.5.2.3	Active Transfer Learning Method and its Comparison with other methods	137
5.5.2.4	Results and Discussion on Complete Image	140
5.6	Conclusions	143
 CHAPTER - VI AUTOMATIC GLAUCOMA DIAGNOSIS FROM DIGITAL FUNDUS IMAGE		 145
6.1	Introduction	145
6.2	The Work in Perspective	145
6.3	Proposed Methodologies	147
6.3.1	Methodology 1: Image processing Disc and cup Extraction for Glau- coma	147
6.3.1.1	Proposed Algorithm	148
6.3.1.2	Experiments and Results	159
6.3.2	Methodology 2: Deep CNN for Glaucoma Diagnosis	164
6.3.2.1	Outline for Deep Learning Convolutional Neural Network	165
6.3.2.2	Proposed Deep Architecture for Glaucoma Classification	168

6.3.2.3	Experiments and Results	170
6.3.3	Methodology 3: Ensemble Learning of Clinical Features and Deep Learning based Classifier	172
6.3.3.1	Clinical Indicators for Glaucoma	173
6.3.3.2	Proposed Algorithm	175
6.3.3.3	Experiments and Results	178
6.3.3.4	Dataset	178
6.4	Conclusions	186
CHAPTER - VII MAIN CONCLUSIONS AND SUGGESTIONS FOR FUTURE WORK		188
7.1	Main Conclusions	188
7.2	Suggestions for Future Work	189
REFERENCES		191
LIST OF PUBLICATIONS		216
BIO-DATA		219

LIST OF FIGURES

Fig. 1.1	Global estimate of people with vision impairment and those with vision impairment that could have been prevented or has yet to be addressed [1].	2
Fig. 1.2	Global number of glaucoma patients as stated by 2019 Vision report of Glaucoma [1]	3
Fig. 1.3	Regional comparison of the total number of people with glaucoma [1]	4
Fig. 1.4	Computer aided diagnosis procedure for glaucoma identification. The image is captured using a ophthalmoscope followed by a glaucoma detection system. The predicted results are displayed on computer screen/device.	5
Fig. 1.5	(a) A cross-sectional view of eye and its anatomical structures, (b) retinal layers	6
Fig. 1.6	(a) An animated healthy retinal (or fundus) image, (b) A real fundus of eye [2]	9
Fig. 1.7	Retinal Images with artifacts and pathological conditions from STARE database	10
Fig. 1.8	A healthy eye view the RGB image as shown in (a) and a glaucomatous eye visualize the image as shown in (b). [3]	11
Fig. 1.9	The image in (a) represents the Open Angle Glaucoma and (b) shows the Closed Angle Glaucoma [4]	14
Fig. 1.10	The camera in (a) shows the hand-held Ophthalmoscope and (b) represents the fundus camera [5]	17
Fig. 1.11	Clinical features of glaucoma	19
Fig. 1.12	Block diagram representing the contributions and structure of the thesis. We exploit various image processing and deep learning techniques for detection, segmentation, and classification tasks.	29
Fig. 1.13	Block diagram representing the methodologies employed for different clinical indicators such as CDR, PPA, RNFL loss, etc depicted in Fig 1.12. We have used various deep learning networks such as U-net, Generative adversarial network (GAN), and pre-trained classification networks (ResNet, Vgg16, etc.) to locate/diagnose the above indicators.	30

Fig. 3.1	A retinal image acquisition procedure can be represented in two ways. The left image shows the Macula centered retinal image used for DR analysis and right represents the optic disc centered retina for glaucoma diagnosis from Messidor and Drions public databases respectively. Details are given in Sec. 3.1.	52
Fig. 3.2	The effect of the decay parameters γ and $\beta \in \{1, 3, 5, 7\}$, for the normalized Distance Map in (a) and the Intensity Map in (b). In the RGB retinal image (the first image in the top row), the green cross represents the annotated Optic Disc (OD) center. Sec. 3.4.1.2 has the relevant details. This also motivates the use of the fused Distance-Intensity (DI) Map.	57
Fig. 3.3	The proposed U-Net-based CNN structure for DI map generation. The U-Net consists of five convolution layers with a sigmoid activation function at the end. The input is an RGB image of dimension 512×512 . Each block has the following operations in sequence: convolution, activation, batch normalization and dropout. The output map gives the probability of association of each pixel to the OD region. Sec. 3.4.1.2 has the relevant details.	58
Fig. 3.4	Tukey's biweight loss function (a) and its derivative (b). We use this robust M-estimator in the loss function of the U-Net architecture to make it robust to outliers: details in Sec. 3.4.1.3. Our experiments show the advantage of using this robust M-estimator. Fig. 3.13 illustrates representative cases of the use of Tukey's biweight function in suppressing exudates and other clinical pathologies.	59
Fig. 3.5	Proposed Architecture for Optic Disc Segmentation	62
Fig. 3.6	Plot shows the (a) horizontal and (b) vertical projection profiles of test and one of the atlas image.	63
Fig. 3.7	SIFT descriptors for test image (a)-(b) and atlas image (c)-(d) respectively.	66
Fig. 3.8	The block diagram representation of the proposed algorithm. It shows the three stages of work:(1) pro-processing and augmentation, (2) adversarial training, and (3) post-processing. Here the solid lines represents the path for training the samples, whereas dashed lines shows the testing image path for disc extraction. Details are given in Sec. 3.5.2.	67

- Fig. 3.9 Pipeline of the proposed architecture. The dashed lines represents the backpropagation losses generated during network training: Adversarial and Segmentation (Reconstruction) loss. Whereas the solid lines shows the serial transfer of data from one block to other. Details are given in Sec. 3.5.2.2. 69
- Fig. 3.10 The generator (segmentation) network (a) based on U-net model. It consists of eight convolution layers in downsample and upsample path. Moreover the discriminator network (b) is of four convolutional blocks to classify between real or fake disc map 70
- Fig. 3.11 It shows the distance map prediction under MSE scenario. In these rows, the first image is the input RGB image, middle is the ground-truth distance map and rightmost is the predicted distance map corresponding to input image. It can be seen clearly that distance map based prediction mis-classifies some of the exudates and background pixels as probable optic disc area for LoG localization. Details in Sec. 3.6.1.2.1. 74
- Fig. 3.12 It shows the distance fused intensity map prediction under MSE scenario. It can be seen clearly that it shows better prediction of map values for poor quality blurred and low illumination images. Although in case of clinical pathology like exudates the distance fused intensity map prediction using MSE fails for corresponding regions as shown in first row of Fig. 3.13. Details in Sec. 3.6.1.2.3. 75
- Fig. 3.13 A comparison of the fused Distance-Intensity (DI) map prediction with mean square error (MSE) and Tukey's biweight loss function (in the training process). The first row shows (a) the input, and (b) the ground-truthed DI map. The second row shows (c) the OD prediction with the DI map with an MSE-based loss function, and (d) the OD prediction with the DI map for Tukey's biweight loss function. This representative example illustrates the outlier rejection property of Tukey's biweight loss function over an MSE-based one. The MSE-based loss function ends up additionally highlighting exudates (which are clinical pathological regions, rather than true OD candidates). The use of Tukey's biweight loss function suppresses these outlier regions significantly, leading to better OD localization. Sec. 3.4.1.3) has the details. 76
- Fig. 3.14 Mean Euclidean distance error (MEDE) for each gamma value has been plotted to choose the optimal parameter. $\gamma = 7$ and $\beta = 7$ has been selected as it gives the minimum EDE for AIIMS private database. Details are given in Sec. 3.6.1.3. 76

- Fig. 3.15 Comparison of mean square error (MSE) Vs Tukey-biweight loss function. Clearly, the Tukey's loss curves for training and validation lies below MSE and thus have better generalization. 77
- Fig. 3.16 Convergence rate comparison between MSE and Tukey's biweight loss functions. MSE loss function require more number of iterations (epochs) to converge than Tukey's, thus offer advantage in terms of computational complexity. Details in Sec. 3.6.1.4. 78
- Fig. 3.17 Some of the sample results with Kaggle as training and AIIMS private retinal images as testing datasets respectively. Here, each row represents an artefact scenario with each location representing the raw input RGB image, middle is the predicted distance-intensity map, and the rightmost shows the marked optic disc location with blue cross. The first row represents the Non-uniform illumination samples, the second row shows the blurred retinal samples, the third row represents the clinical artefacts like exudates or hemorrhages etc. and the last row represents some other set of the challenging images encountered while validating the model. Details are in Sec. 3.6.1.5. 79
- Fig. 3.18 Sample images from (a)-(d) belong to Drions, (e)-(f) Drishti and (g)-(h) Rim public dataset for Optic disc segmentation. Here green and black colour represents the proposed and expert boundary respectively 82
- Fig. 3.19 The bar plot represents the three performance parameter i.e., Dice metric, disc overlap and sensitivity (in percentage) for various discriminator losses. The image is visualized better in RGB color-space. Details are given in Sec. 3.6.2.2.3. 89

Fig. 3.20 Some representative examples of test images from all the databases. Here the red and blue line markings show the ground-truth and predicted markings for optic disc boundary. In the first row (A) the optic disc image is affected by clinical atrophy named peripapillary atrophy (PPA) where the texture and color of pixels just outside the disc boundary varies from the background. It makes the segmentation procedure more complex due to the large variation of pixel characteristics. In the second row (B) each disc boundary is diffused into the background, thus makes the segmentation process tough. In spite of this, the proposed algorithm is able to segment the disc precisely. Lastly, the third column (C) shows oval-shaped discs from the Drions dataset with different color representations. (D) some other challenging images with pathology and artifacts. Details are given in Sec. 3.6.2.2.3. 91

Fig. 4.1 The proposed Y-net architecture with ResNet34 model as main and EfficientNetB0 as side encoder for optic cup segmentation. At the bottleneck layer inception and context block are added to capture the cup of all sizes and also to maintain the spatial consistency of pixels in feature maps. The right side of architecture shows the decoder path that restores the feature maps back to the original image dimension. Moreover, the blue and violet color encoder and decoder subblocks have been shown (right bottom), here BN is batch normalization, Conv is convolution, and ReLU is rectified linear unit activation function. Also, the dark brown subblocks in decoder path represents the up-sampling operation. It is to noted that the lowest resolution of encoder is 16×16 pixels. Sec. 4.3 has the relevant details of the network and subblocks. 97

Fig. 4.2 The top inception bock consists of three parallel convolution operations, with each path having different receptive field dimension in order to capture the multi-size optic cup region. Next, the context block at the bottom extracts the contextual information from the semantic features and also maintain the spatial consistency of feature map. Details are given in Subsec. 4.3.3.1 and 4.3.3.2 respectively. 98

Fig. 4.3 It shows the conventional U-net at the top and its variant Y-net with two encoder and one decoder architecture at the bottom. Details in Sec. 4.3.2.2. 100

- Fig. 4.4 Representative examples of success in the Drishti-GS [6] and Refugee datasets. Moreover, the results have been shown on the extremely challenging AIIMS Community Camp dataset. The AIIMS Community Camp dataset has images taken in poor lighting conditions, using hand-held ophthalmoscopes. The rows show representative examples of the success of correct OC boundary estimation in images from (a) Drishti-GS, (b) Refugee, (c) AIIMS, and (d) other miscellaneous challenging examples. Sec. has the details. The red and blue circles represent the ground-truth and predicted cup margins respectively. Details are present in Sec. 4.4.3 107
- Fig. 5.1 Some sample retinal images under non-uniform or poor lighting conditions. The first column (images obtained from Drions dataset [7]) corresponds to a healthy retinal image at the top and its corresponding cropped optical disk (OD) region, below. The second and third columns represent PPA images and their corresponding cropped OD regions collected from a private community camp dataset (All-India Institute of Medical Sciences (AIIMS, hereafter), New Delhi). The PPA region in the image (marked with a white arrow) should be detected by a CAD system. 111
- Fig. 5.2 The complete pipeline for the proposed work representing three major steps:(a) Region of Interest (ROI) Extraction, (b) Data Augmentation, (c) Feature extraction from pre-trained ResNet50 [8] and a statistical model, and lastly, (d) concatenation of features and training of the final dense layers: Details in Sec. 5.3.1. 115
- Fig. 5.3 ResNet50 [8]-based proposed architecture for PPA classification. The upper block represents the pre-trained layers from the ResNet50 model on the ImageNet dataset. The lower block represents the clinically statistical features extracted from ROI. We concatenate features from both models to generate a 2117-dimensional feature vector. We finally train the dense layers (at the right) for binary classification. Our experimentation in Subsec. 5.5.1.3 shows that the combination of deep features and these clinically significant features outperforms any of the individual models. 118
- Fig. 5.4 Details of the CONV and IDEN blocks from the overall proposed network of Fig 5.3. These blocks contain shortcut connections which help to deal with the vanishing gradient problem in deeper connections. The upper block contains convolution operations and lower consists of the identity skip connections. 119

- Fig. 5.5 It represents the detailed block diagram of the proposed work for RNFL defect detection. The first four blocks which are blood vessel extraction, inpainting, red-free channel enhancement and patch generation with augmentation depicts the pre-processing steps required before training the network. Next block performs the training on patches with pre-trained VGG16 network in active learning framework. Lastly for the tested complete image, a condition on ratio of predicted RNFLD to total tested patches is applied to avoid any false positives in final image prediction. Details are given in Section. 5.4. 123
- Fig. 5.6 It shows the detailed pre-processing steps of the work. In the first row it starts with a RGB image as input, extracted binary blood vessels, inpainted RGB image. Next in second row green channel inpainted image, equalized green channel inpainted image and extracted RNFL defect patches in red square are shown. Details are given in Subsection. 5.4.1.1-5.4.1.2 . 125
- Fig. 5.7 The stage diagram of proposed active transfer learning (ATL) method for RNFL defect detection from patch based training samples using VGG16 pre-trained network. Here input training image is a patch with $64 \times 64 \times 3$ pixel dimension and consists of three channels (red-free). The channels are green, blue and contrast green channel. Details are given in Sec.5.4.2 127
- Fig. 5.8 The figure shows the test patches extracted from the region of interest for image level testing of RNFL loss. The optic disc center is marked with blue cross, the ROI is a circular region shown around the optic disc with red circle and finally the extracted patches for testing of 64×64 pixel dimension and 50% overlapping. Details are given in Sec.5.4.3 128
- Fig. 5.9 The proposed method performs well for a wide variety of difficult PPA pathology variations, which includes impressive performance on a community camp-based dataset with poor illumination, poor sitting conditions and low-resolution hand-held ophthalmoscopes. The first row shows difficult cases with a wide variety of PPA textures. (The text box below each figure shows the corresponding PPA probability as estimated by our method.) The second row shows retinal images with poor resolution due to blurring or other motion artefacts. Sec. 5.5.1.3 has the details. 131

- Fig. 5.10 A representative example of successful PPA detection (a) in spite of high illumination, and some noise as well. In this case (b), the ResNet50 model-based features gives low probability value of 0.479 and mis-classifies it as healthy. The statistical features are relatively unaffected by the high illumination (a probability value of 0.66). The proposed fused feature technique enables the successful classification with a probability values of 0.78. 132
- Fig. 5.11 An example of another difficult query image(healthy), with some dark texture around the optic disc (a). The ResNet50 model mis-classifies this as a PPA case. A classification with clinically statistical features correctly classifies this as a healthy case. The proposed fused feature technique enables the successful classification with the minimum PPA probability among the three (0.009), which indicates a healthy eye. The adjoining bar plot (b) indicates the relative PPA probability scores corresponding to the three methods. 132
- Fig. 5.12 A representative example (a) of the proposed fusion technique succeeding when deep features and statistical features individually misclassified the image. This is a difficult-to-classify example of a healthy eye. Both statistical features and ResNet50 individually failed to classify the query image as Healthy (b). Here, the fusion strategy works with a PPA probability score of 0.12 (and a consequent Healthy Eye probability of 0.88). Sec. 5.5.1.3.1 has the details. 133
- Fig. 5.13 Successful classification on some representative challenging images: The first row shows the query PPA images collected from community camps. The second row represent the healthy images from publicly available datasets. The probability scores shows the successful classification in spite of blurry/varied pathological cases. The text box shows the PPA detection probability from our proposed fusion approach, and the ground truth(GT) marking by experienced ophthalmologists. Details in Sec. 5.5.1.3.1. 134
- Fig. 5.14 Implementation details: No over-fitting. The graphs above show the loss (a) and accuracy (b) performance of our PPA classification for training and validation data with each epoch. The model clearly learns the data without any over-fitting. More details are in Sec. 5.5.1.4. 135

- Fig. 5.15 The plot shows the number of training samples at each iteration of active learning method Vs test accuracy of patch-based learning. It clearly shows that as the number of labelled samples increases in training set the test accuracy increases. Details are given in Sec.5.5.2.2 138
- Fig. 5.16 The bar plot shows the effect of various selection criterion's on the test accuracy. It shows that high entropy criterion when used for sample selection gives best test accuracy of 97.75% over other metrics. Details are given in Sec.5.5.2.2. 138
- Fig. 5.17 The graphs above show the (a) accuracy and (b) the loss performance of our RNFL patch classification for training and validation data with each epoch. The model clearly learns the data without any over-fitting. More details are in Sec. 5.5.2.3. 140
- Fig. 5.18 The figure shows the complete test image, from where testing patches are generated and fed input to the model for testing. The blue color dotted squares represent the predicted RNFL defect regions and the red shows the ground-truth RNFL defect areas. It can be seen that most of the predicted patch overlap with GT and thus gives high sensitivity. Details are given in Sec.5.5.2.2 142
- Fig. 5.19 Comparison of FROC curves for different RNFLD detection algorithms. Details are given in Sec.5.5.2.4 143
- Fig. 6.1 The figure (a) shows a sample retinal (or fundus) image. It consists of three major anatomical structures i.e. optic disc (optic cup inside it), macula and blood vessels. An enlarged version of optic nerve head (ONH)/optic disc has been shown in (b) with expert annotated optic disc (OD) and optic cup (OC) boundaries. The healthy image shows a orange color neuro-retinal rim (NRR) region between cup and disc. Details are given in Sec. 6.1. 147
- Fig. 6.2 The block diagram shows the complete pipeline of proposed algorithm. It takes the RGB retinal image of dimension 605×700 pixels as input and perform various pre-processing steps to highlight the significant features such as blood vessel extraction, vessel inpainting, image enhancement etc. A series-wise implemented steps include optic disc segmentation using chanvese based active contour, optic cup segmentation with multi-thresholding and vessel bending information. In the last step of proposed algorithm, CDR and ISNT parameters are used to classify the image into glaucoma or normal. Details are given in Sec. 6.3.1.1. 148

- Fig. 6.3 Curve C propagating in two-dimensional space along normal direction. Details are given in Sec. 6.3.1.1.2. 150
- Fig. 6.4 (A) The input RGB image is pre-processed to extract (B) Red channel image with an (C) initial circular mask (red circle) and (D) finally active contour is applied which results into a curve fitted to the optic disc boundary. At last image (E) gives the segmented binary disc OD. Details are given in Sec. 6.3.1.1.2 152
- Fig. 6.5 Some sample glaucoma images that shows pallor region marked with blue color for cup segmentation. As the disease progresses the pallor color becomes yellowish-white. Details are given in Sec. 6.3.1.1.3.2. 155
- Fig. 6.6 Retinal blood vessel in-painting for pallor region extraction in RGB images. The top left image represents the cropped RGB image with extracted region of interest for cup segmentation and bottom left corresponds to vessel-inpainted RGB image. The blood vessels have been fused into the background which clearly brings out the margin between cup and rim regions. The idea is to blend the vessel colour into the cup to create a smooth intensity region inside cup for thresholding. Moreover, the second column shows the thresholded outputs corresponding of images with no and inpaint images. Details are given in Sec. 6.3.1.1.3.2. 155
- Fig. 6.7 It shows the Step 1 and 2 of the cup segmentation algorithm. The input RGB image after global multi-thresholding gives a segmented image in color space (second image from left), along with the high intensity pixels shown in red color along with blood vessels surrounding it (third image from left). Finally the resulted convex hull operated binary image (last image) gives initial estimate for cup region. Details are given in Sec. 6.3.1.1.3. 156
- Fig. 6.8 The series-wise implemented steps (Step 3-7) for cup segmentation includes (a) vessel cleaning: hair-like vessel trimming, remove small vessel segments, remove nearby branch points etc. (b) significant branch point selection based on criterion (c) Fit a best possible circle to all extracted branch points in all sectors (d) use Coarse-to-fine multi-thresholding information to refine the cup boundary. Details are given in Sec. 6.3.1.1.3. 158

Fig. 6.9	It shows some of the sample results for disc and cup segmentation. The black circles corresponds to proposed disc (outer) and cup (inner) boundaries. The dotted circles in red, green and blue shows the three expert marked cup boundaries. Moreover, the vessel bend points are also shown with blue circles which gives the close estimate to true cup margins. Details are given in Sec. 6.3.1.2.2.	162
Fig. 6.10	Proposed CNN architecture for glaucoma diagnosis	166
Fig. 6.11	Loss (a) and Accuracy curves (b) for the proposed CNN as glaucoma classifier	171
Fig. 6.12	CNN prediction score for Glaucoma. (a) Score for true glaucoma images and (b) true healthy retinal images.	172
Fig. 6.13	Pipeline for Glaucoma Diagnosis. Details in Sec. 6.3.3.2.	173
Fig. 6.14	Categories of Glaucoma datasets. The left image shows the category A database image which has optic disc centered retinal images from the Rim-one dataset. On the right side the B category database are represented by a full size retinal images extracted from ORIGA database. Details in Sec. 6.3.3.4.	179
Fig. 6.15	ROC curve for Drishti dataset with six standard pre-trained CNN networks.	182

LIST OF TABLES

Table. 3.1	Detailed Retinal Image datasets. Description is given in Sec. 3.6.1.1	72
Table. 3.2	The evaluated test accuracy for each database with different train and test combinations. The first three rows show the individual dataset being trained and tested. It has been observed that the Drive, Drions, Stare, and Drishti perform better when trained with Messidor rather than with Kaggle. Whereas the AIIMS private database gives 5.08% better accuracy rate when trained with Kaggle images.	80
Table. 3.3	The proposed approach has compared the performance parameter (accuracy) with state-of-art methods for Messidor database under 1R and 1/2R regions. Details in Sec. 3.6.1.6.	81
Table. 3.4	Proposed optic disc segmentation algorithm performance parameters for different databases	83
Table. 3.5	Comparison of methods for optic disc segmentation for DRIONS Database. The symbol "-" represents no result has been reported for the case	84
Table. 3.6	Comparison of methods for optic disc segmentation for RIM Database. The symbol "-" represents no result has been reported for the case	84
Table. 3.7	Comparison of methods for optic disc segmentation for DRISHTI-GS Database. The symbol "-" represents no result has been reported for the case	84
Table. 3.8	Detailed Optic Disc Retinal Image Segmentation datasets	85
Table. 3.9	It shows the three performance parameters sensitivity, overlap and dice metric values with different gan2seg loss tuning parameter (γ) for Drishti-GS1 database. It implies the trade-off between the adversarial and segmentation losses. Details in Sec. 3.6.2.2.3.	86
Table. 3.10	Dice metric based confusion Matrix of 8 different databases. The bold values represent the numbers selected to give the maximum possible average dice metric for combined test images when trained with four datasets i.e Riga-BinRushed, Drishti-GS1, Refugee and Rim-One. Details are given in Sec. 3.6.2.2.3.	87
Table. 3.11	Optic disc overlap based confusion Matrix of 8 different databases. The bold values represent the numbers selected to give the maximum possible average overlap for combined test images when trained with four datasets i.e Riga-BinRushed, Drishti-GS1, Refugee and Rim-One. Details are given in Sec. 3.6.2.2.3.	88

Table. 3.12	The three major performance parameters i.e., sensitivity, disc overlap and dice metric used for evaluating the performance of proposed generative adversarial network for eight different datasets. Details are given in Sec. 3.6.2.2.3.	89
Table. 3.13	The proposed approach has compared the performance parameter (sensitivity, overlap and dice metric) with state-of-art methods for Drishti-GS1 database. Details in Sec. 3.6.2.2.4.	92
Table. 3.14	The proposed approach has compared the performance parameter (sensitivity, overlap and dice metric) with state-of-art methods for Refugee database. Details in Sec. 3.6.2.2.4.	92
Table. 4.1	All the optic cup segmentation datasets with image count and dimension. For experimentation purpose we have used four public and one private dataset. Details are given in Sec. 4.4.1.	103
Table. 4.2	To evaluate the performance of the algorithm, the validation results for different architecture has been shown for Drishti-GS dataset. All three performance parameters (sensitivity, overlap and dice metric) are given below to compare different models. Details in Sec. 4.4.3.	105
Table. 4.3	The proposed approach has reported the performance parameter (sensitivity, overlap and dice metric) for all four public databases i.e Drishti-GS1, Refugee, Drive, Stare and one private dataset collected from AIIMS, New Delhi. Details in Sec. 4.4.3.	106
Table. 4.4	The proposed approach has compared the performance parameter (sensitivity, overlap and dice metric) with state-of-art methods for Drishti-GS database. Details in Sec. 4.4.4.	108
Table. 4.5	The proposed approach has compared the performance parameter (sensitivity, overlap and dice metric) with state-of-art methods for Refugee database. Details in Sec. 4.4.4.	108
Table. 5.1	In the proposed architecture (Fig. 5.3, the layers till CONVb+(IDENx2) have been pre-trained on ImageNet database. The 2048-dimensional extracted features are concatenated with a 68-dimensional clinically significant statistical feature vector, to generate a 2117-dimensional full feature vector. Towards the right of Fig. 5.3, a fully connected layer of 128 neurons is added, followed by one with a sigmoidal activation function. The classification training is performed only for last layers and rest are frozen i.e., no weight updating is done for them.	120

Table. 5.2	<p>Details of the seven Retinal Image datasets for PPA. The first six are publicly available. The last is a private one, which we have used for validation. This is a rather challenging one, collected from community camps of AIIMS, New Delhi. This has images captured under poor lighting conditions, poor sitting setups, and low-resolution hand-held ophthalmoscopes. All images have been manually marked by an experienced ophthalmologist from AIIMS. Sec. 5.5.1.1 has the details.</p>	129
Table. 5.3	<p>This table summarizes experimentation performed with various augmentations methods. We have experimented with standard geometric transformations such as rotation, flipping, motion blur, shear etc. both individually, as well as with combinations of the same. To enhance the variability of the training data, we have also experimented with color/grey level-based transformations such as unsharp masking, blurring and noise. A combination of unsharp, noise, motion blur, and vertical flip gives the best performance among all types. Sec. 5.5.1.2 has the details.</p>	130
Table. 5.4	<p>Performance comparison with state-of-the art methods. The first four methods are based on statistical features. The last-but-one is based on a deep learning model using pre-trained weights. The last method is the proposed fusion of statistical and deep network features. Sec. 5.5.1.5 has the details.</p>	135
Table. 5.5	<p>Details of the RNFL dataset patches. Each image has been manually marked by an experienced ophthalmologists from AIIMS. The RNFL defect and background patches have been split-ed into approximately 9:1 train-test ratio. Sec. 5.5.2.1 has the details.</p>	137
Table. 5.6	<p>Effect of patch size of input training data. As patch size increases test accuracy increases. Also, the training image patches have been augmented with flipping, rotation and zooming operations. Sec. 5.5.2.2 has the details.</p>	139
Table. 5.7	<p>A comparison with Transfer and active learning has been performed with Vgg16 architecture as the backbone network. In the first row, TL gives an average accuracy of 73% whereas the active learning results into much better average accuracy of 93.2%. In the final experiment a combination of transfer and active learning approaches has been performed and it gives an overall increase in test accuracy with a value of 97.2%.</p>	139

Table. 5.8	The table shows some comparison of proposed method with other works and architectures as the backbone for the experimentation. The first row represents a 7-layer CNN trained on red-free patches with obtained average accuracy of 92.94%. Further the network of [9] has been used along with AL framework which leads to increase in accuracy by 2.56%. Similarly, third row represents ResNet34 architecture as backbone and generates an accuracy of 95.78%. Details are given in Sec. 5.5.2.3.	140
Table. 5.9	A "Leave-one-out" test method has been employed in the given table due to limited database. The columns from second to fifth shows the TP, TN, FP and FN values used to calculate the performance measures shown in Table 5.10. Each row represent a set which has been trained on 12 images and tested on the first column image. The last two column shows the predicted and true label of the overall image based on 30% criterion mentioned in detail in Sec. 5.5.2.4. Here 1 corresponds to RNFL defect and 0 to background patch respectively.	141
Table. 5.10	Performance comparison of Retinal nerve fiber layer defect (RNFLD) in fundus image with other state-of-art methods. Details are given in retinal Sec. 5.5.2.4.	143
Table. 6.1	The table shows performance comparison of proposed algorithm to other methods for optic disc segmentation on Rim dataset. Sec. 6.3.1.2.3 has the details.	160
Table. 6.2	The table shows performance comparison of proposed algorithm to other methods for optic disc segmentation on Drishti-GS1 dataset. Sec. 6.3.1.2.3 has the details.	163
Table. 6.3	The table shows performance comparison of various methods for optic cup segmentation on Drishti-GS1 dataset. The experiment has been performed on 101 images of publicly available Drishti-GS1 dataset. The performance parameters like sensitivity, specificity, optic cup overlap and dice metric has been shown in the table for other methods and the proposed methodology. Sec. 6.3.1.2.3 has the details.	164
Table. 6.4	Confusion matrix for Glaucoma analysis on Drishti-GS1 dataset of 101 images. The algorithm classifies each image into glaucoma or normal. Each image has expert marked labelling corresponding to one of these two class. Sec. 6.3.1.2.2 has the details.	164
Table. 6.5	Detailed architectural design for the proposed CNN	169
Table. 6.6	Detailed glaucoma public datasets	170

Table. 6.7	Detailed results for Glaucoma classification on Refugee, Drishti-GS, and HRF public datasets	171
Table. 6.8	The obtained performance parameters such as sensitivity, specificity, positive predictive value, accuracy, and F1-score on the Drishti-GS database	171
Table. 6.9	All the public glaucoma datasets with image count and dimensions. Details are given in Sec. 6.3.3.4.	179
Table. 6.10	Six major State-of-art deep convolutional networks that has been experimented on Drishti-GS1 dataset with 80% training, 10% validation and 10% testing respectively. All layers have been fine-tuned after the warm-up of last dense layers using pre-trained weights of Imagenet database.	182
Table. 6.11	Different networks trained and tested individually on each dataset. The values shows the accuracy and area under the curve performance parameters.	183
Table. 6.12	Performance parameter comparison of Ensemble learning approach with pre-trained deep network and CDR based classification approach for Drishti dataset.	185
Table. 6.13	Performance parameter comparison of Ensemble learning approach with pre-trained deep network and CDR based classification approach for Origa dataset.	186
Table. 6.14	Performance parameter comparison of Ensemble learning approach with pre-trained deep network and CDR based classification approach for Rim dataset.	186
Table. 6.15	Significance of RNFL loss and PPA clinical indicators in glaucoma diagnosis	187

LIST OF ABBREVIATIONS

OD	Optic Disc
RNFL	Retinal Nerve Fiber layer
WHO	World Health Organization
VHI	Vision Health Initiative
CDC	Center for Disease Control and Prevention
AMD	Age related Macular Degeneration
DR	Diabetic Retinopathy
IAPB	International Agency for the Prevention of Blindness
CAD	Computer Aided Diagnosis
OCT	Optical Coherence Tomography
ONH	Optic Nerve Head
FOV	Field of View
IOP	Intra Ocular Pressure
VFT	Visual Field Test
CFP	Colored Fundus Photographs
NTG	Normal Tension Glaucoma
NEI	National Eye Institute
HRT	Heidelberg Retinal Tomography
CDR	Cup-to-Disc Ratio
PPA	Peripapillary Atrophy
NRR	Neuro Retinal Rim
ISNT	Inferior Superior Nasal Temporal
ML	Machine Learning
GT	Ground Truth
PCA	Principal Component Analysis
SVM	Support Vector Machine
KNN	K-Nearest Neighbor
ROI	Region of Interest
CNN	Convolutional Neural Network
CHT	Circular Hough Transform

LIF	Local Image Fitting
DCNN	Deep Convolutional Neural Network
BN	Batch Normalization
CCE	Categorical Cross-Entropy
CRF	Conditional Random Field
CFI	Colored Fundus Image
CSD	Coupled Sparse Dictionary
CCA	Canonical Correlation Analysis
CV	Chan-Vese
FCM	Fuzzy c-Means
SWFCM	Spatially Weighted Fuzzy c-Means
LS	Least Square
MSE	Mean Square Error
MAE	Mean Absolute Error
SLIC	Simple Linear Iterative Clustering
GAN	Generative Adversarial Networks
SGD	Stochastic Gradient Descent
RBF	Radial Basis Function
LDA	Linear Discriminant Analysis
LBP	Local Binary Pattern
GLCM	Gray Level Co-occurrence Matrix
HOG	Histogram of Gaussian
BIF	Biologically Inspired Features
LOG	Laplacian of Gaussian
CLACHE	Contrast Limited Adaptive Histogram Equalization
ACC	Accuracy
ROC	Receiver Operating Characteristic
AUC	Area Under Curve
DRIVE	Digital Retinal Images for Vessel Extractions
DRIU	Deep Retinal Image Understanding
DDL	Disc Damage Likelihood Scale